Article

Automotive Fuel Cell Systems: Testing Highly Dynamic Scenarios

Jonas Breitinger [1],* , **Mark Hellmann [1]** , **Helerson Kemmer [1]** and **Stephan Kabelac [2]**

1   Robert Bosch GmbH, 71272 Renningen, Germany
2   Institute of Thermodynamics, Leibniz University Hannover, 30823 Garbsen, Germany
*   Correspondence: jonas.breitinger@de.bosch.com; Tel.: +49-711-811-11430

Abstract: PEM fuel cell systems face highly dynamic load profiles in automotive application. This work showcases the impact of media supply adaption, system architecture and test rig restrictions on the transient voltage response of an automotive fuel cell stack. Current step and load profile experiments were conducted on a system test rig, featuring automotive balance of plant components, and a short stack test bench. A time scale analysis allowed us to identify the predominant effect for the voltage response in each test case. The voltage response measured in the test cases was dominated either by air supply, membrane humidification or coolant temperature dynamics. This systematic comparison of different types of test setups highlights the importance of application-like system level testing as, in contrast to common experiments, different phenomena shape the electrical stack behavior.

Keywords: PEM; fuel cell system; dynamic operation; experimental

1. Introduction

Polymer Electrolyte Membrane Fuel Cells (PEMFCs) offer a promising way to achieve carbon dioxide-free transportation in the near future. A big step towards widespread application of PEMFCs in passenger cars has been taken with the launches of Hyundai's ix 35 Fuel Cell and Toyota's Mirai FCV in 2013 and 2014, respectively [1,2]. However, significant research is necessary for market breakthrough, to, e.g., increase power density and lifetime and reduce cost as formulated by the United States Department of Energy (DoE) [3].

To achieve these requirements, understanding of water management in PEMFCs is crucial. The proton conductivity of the membrane is highly dependent on its water content [4–7]. For a high cell efficiency, one has to ensure a sufficiently high membrane water content during operation to minimize the membranes ohmic resistance. On the other hand, states in which liquid water blocks the reactant transport and affects the function of the catalyst layer have to be avoided as well. Both states, too dry and too wet, lead to a decrease in performance and lifetime [8].

In automotive applications, the fuel cell systems face highly dynamic load profiles, which is represented in benchmarking cycles such as the Worldwide harmonized Light vehicles Test Cycle (WLTC). In addition, a customer expects a certain driving performance, for example, a certain top speed and acceleration. The exact values depend on the vehicle class. From the vehicle performance requirements, the Fuel Cell System (FCS) requirements in terms of steady-state net power and dynamics can be derived. The electrical net power requirements can be calculated from a vehicle simulation, by modeling air resistance, friction losses, motor and inverter losses for a selected vehicle type. Typically, fuel cell systems are combined with a low capacity battery for the fuel cell system start-up and for energy recuperation via the electrical motor during driving. In a fuel cell dominant approach, the steady-state power has to be produced by the fuel cell system. This leads to a relatively low capacity battery.

However, the fuel cell system must provide a high net power in a short time, to fulfill the acceleration requirements. If one would design a vehicle with a battery large enough to supply the whole net power necessary for this case, a high capacity battery had to be installed, as power-to-energy ratios (P/E) of batteries are limited. If the battery is only used for start-up and boost operation, the required energy content is not the dimensioning factor. For a fuel cell dominant vehicle, the maximum power becomes relevant. In this case, a high-power battery with a large P/E ratio is chosen over a high energy battery. The European Council for Automotive R&D (EUCAR) states a P/E of $7.5\,\text{h}^{-1}$ for state-of-the-art Plug-in Hybrid Electric Vehicle (PHEV) batteries during a $10\,\text{s}$ peak load [9]. Therefore, a cost advantage can be achieved when the fuel cell system can deliver the required power P_{req} during transients mainly on its own. It is known from Lohse-Busch et al. [10] that in Toyota's Mirai vehicle, the majority of the power demand during acceleration is provided by the fuel cell system. The Mirai's battery is rather small in capacity ($1.6\,\text{kW h}$), providing a maximum electrical power of only around $20\,\text{kW}$—a fraction of the fuel cell system's power [10].

An exemplary required power curve P_{req} is shown in Figure 1. In this work, the net power of the FCS P_{FCS}, together with the battery's power P_{bat}, should add up to 90% of the FCS's maximum net electric power within $0.8\,\text{s}$. If the fuel cell system's dynamic is enhanced, a lower capacity battery is sufficient to fill the remaining gap in power. In this example, by decreasing the fuel cell system's response time by a factor of four from $6.4\,\text{s}$ to $1.6\,\text{s}$, the battery's capacity can be reduced by a factor of three. Reducing the battery's capacity also reduces the overall system cost.
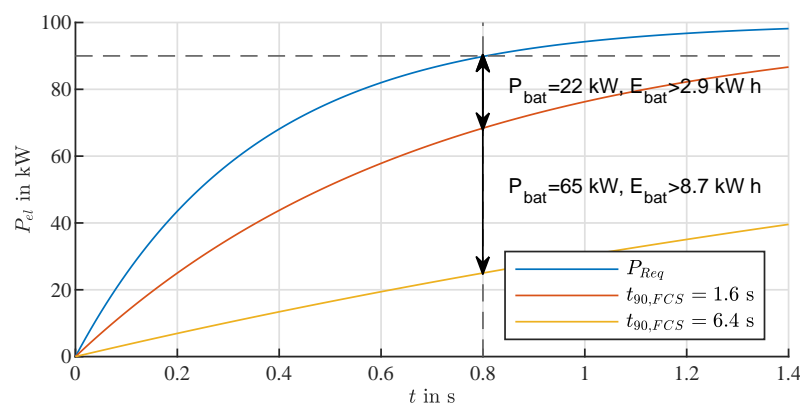

Figure 1. Exemplary power split and resulting battery capacity depending on the fuel cell systems dynamics.

The required electric power changes dynamically during a typical passenger car driving cycle. Therefore, a fast adaption of the fuel cell system's operating point becomes necessary. Every operating point requires a certain optimized set of stack conditions to achieve an ideal hydration state and high system efficiency [11]. This makes a fast adaption of the stack conditions critical to achieve a highly dynamic fuel cell operation.

High potential is also a known factor that accelerates ageing [12]. This can be avoided by so called voltage clipping, limiting the minimal current to approximately 5% of the rated current during operation. Therefore, the oxygen and hydrogen consumption changes by a factor of 20, between 5% and 100% of the consumption at the rated current. A fast increase in load requires a fast adaption of the gas supply mass flows to avoid reactant starvation, which would lead to a performance decrease and accelerated aging [12]. To validate, e.g., a simulation model with highly dynamic, application-like experiments, the mass flow dynamics have to match the targeted fuel cell dynamics. If the mass flow adaption is significantly slower than the targeted fuel cell dynamics, one common way is to set the mass flow as constant [13].

In the case of an upward load step, the mass flow would be set to satisfy the fuel cells' consumption at the higher load. This leads to an unrealistically high stoichiometry at the

initial, lower load and a possibly too-dry membrane: As the high mass flow combined with low water production rates reduces the local relative humidity, the membrane water content is decreased. Typical operational cathode stoichiometries lie between 1.2 and 6. If these operational stoichiometries are used, the fixed mass flow setup limits the achievable current step size to approximately a factor of five. This in turn makes it impossible to realistically validate a load step from idle to max load, where a step size factor of approximately 20 is typical, as described in the previous paragraph.

This is also the case for other stack conditions such as gas pressure and temperature, and coolant mass flow and temperature: If the adaption of these parameters does not match the targeted dynamics, at least one unrealistic operating point occurs. The impact of a delayed condition adaption on the cells' voltage response to a current step has been shown by Loo et al. [14] using a numerical fuel cell model. This finding highlights the relevance of the condition adaption dynamics when evaluating a fuel cell systems response to a load change.

Current steps lead to a voltage overshoot in the case of a current decrease and a voltage undershoot in the case of a current increase, as experimental and simulation literature data suggests [13–21]. A similar behavior is reported for step changes in voltage and the current response [22,23]. Wang and Wang linked it to the transient behavior of membrane hydration, electrochemical double-layer capacitance and reactant diffusion [15]. The time constants of the double-layer capacitance effect is, however, too low to explain the behavior observed in the later sections. In the opinion of the authors, membrane hydration and reactant supply dynamics should be in focus. To investigate this properly, this paper is based on experiments with realistic coolant temperature and reactant supply response times, other than the most common literature experiments.

Tang et al. [24] conducted dynamic experiments with a 1.2 kW fuel cell system. While it is shown that the mass flow adaption works sufficiently fast (<2 s) to allow a dynamic duty cycle, the stack temperature reacts quite slowly (>100 s). This temperature effect dominates the stacks voltage response. In typical automotive systems, a thermal system would be able to adapt significantly faster to the change in heat production, leading to a lower voltage response time constant as shown later in Section 3.4.

As described beforehand, most research either focuses solely on simulation approaches, which are hard to validate without experiments, or on experiments with constant or low-dynamic stack boundary conditions. However, the realistic adaption of stack boundary conditions as well as system or test rig limitations greatly influence the voltage response of a fuel cell stack in highly dynamic operation, as the response in each case is dominated by different effects. To evaluate and optimize control strategies for automotive application and to validate simulation models, realistic experiments are necessary. This work compares typical simplified experiments from the literature with two sophisticated, application-like operated fuel cell systems, highlighting the pitfalls of commonly-used setups regarding transferability towards automotive usage. The key contribution of this paper is the systematic comparison of these experimental setups in dynamic operation, as system level experimental data are especially sparse in the common literature.

This paper is structured as follows: Section 2 introduces the key variables for the experiments, the experimental systems and test rigs, as well as three selected test cases. In Section 3, the impact of load-dependent stack boundary condition adaption, system architecture choice and test rig behavior on the dynamic voltage response is compared. Section 4 focuses on the different root causes dominating the voltage response in the selected test cases. In Section 5, the results are summarized, highlighting their scientific and practical importance. Additionally, topics with further need for research are proposed.

2. Experimental Methods

2.1. Variable Selection

The electrical performance of the stack is evaluated via the stack voltage and current, which are measured at the load, a four-quadrant power supply. During all measurements,

the current is controlled to a certain set point, while the measured stack voltage is primordially a result of current, membrane hydration, gas supply and temperature. An overview of the most relevant effects and their coupling is shown in Figure 2. Note that not all possible effects such as, e.g., current density redistribution, condensation/evaporation and liquid water transport dynamics, are addressed within this work but just the ones in the relevant time scales.
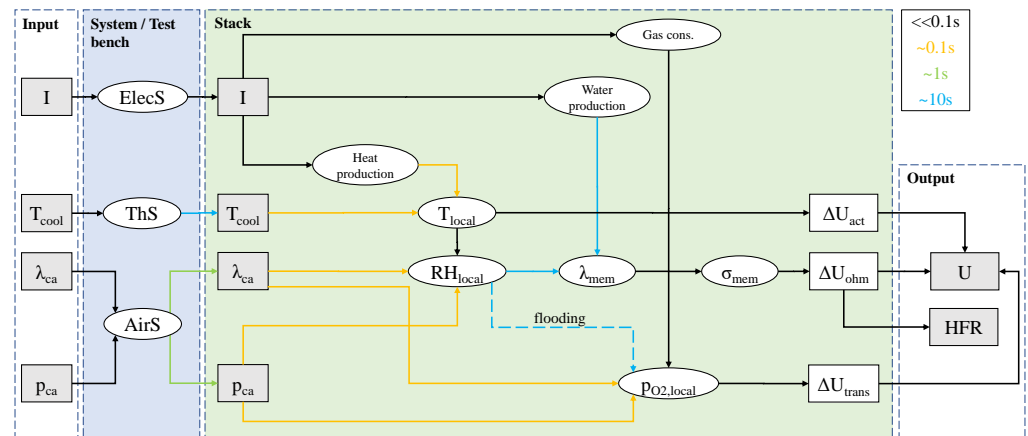

Figure 2. Process chain showing selected variables, their interaction and typical time-scales in automotive systems.

It has to be emphasized that the stack inlet conditions are influenced by the system or test bench characteristics. The set points for certain variables, given as inputs in Figure 2, are only reached with a certain time delay as indicated by the arrow color. The current reaches its set point within a time frame that can be considered instantaneous compared to the other considered effects. Slower responses are typically measured for the air inlet conditions and coolant temperature, depending on the respective subsystem capabilities. In the following lines, the impact of the inlet conditions on the stack's response is discussed.

The gas supply influences the local partial oxygen pressure p_{O_2}, as shown in Figure 2, and the membrane water content λ_{mem} via the local relative humidity RH. This impacts the measured voltage U via a change in membrane conductivity σ_{mem} and the resulting ohmic loss ΔU_{ohm} [25]. If liquid water occurs, a blockage of the gas diffusion paths may result in a significant loss in local reactant partial pressure, as depicted by the dashed arrow in Figure 2.

Due to the higher mass flows and larger changes in the relative humidity along the cathode channel, the cathode pressure p_{ca} and stoichiometry λ_{ca} yield the highest impact on the water management and the cells' performance. The anode stoichiometry and pressure have a minor influence on the water management. In the systems described in Section 2.2.1, the pressure and mass flow dynamics within the Hydrogen System (HyS) exceed those of the Air System (AirS) by far, as hydrogen is supplied from a high pressure tank. Therefore, anode pressure and stoichiometry are neglected for the further analysis and are not shown in Figure 2. For a possible system efficiency analysis it must be noted that especially fast load reductions might require additional purging to quickly reduce the anode pressure, which leads to additional hydrogen losses.

Because of the high thermal conductivity and relatively low thickness of the cell layers in combination with the high coolant heat capacity flux, the cells' local temperature is dominated by the coolant temperature T_{cool} and the heat produced by the fuel cell reaction, as shown in Figure 2. The local temperature influences the local relative humidity severely via the vapor pressure curve: Antoine's equation approximates an exponential relationship between saturation pressure and temperature. Like the gas supply, the temperature impacts the ohmic losses ΔU_{ohm} [6] via the membrane water content. The local temperature also influences the activation losses instantaneously [25].

To distinguish ohmic losses from activation losses ΔU_{act} and mass transport losses ΔU_{trans}, the High Frequency Resistance (HFR) is recorded by the four-quadrant power supply, as depicted on the lower right side of Figure 2. In this work, the real part of the impedance is measured while adding an alternating current with an amplitude of 10 A at a frequency of 300 Hz onto the steady-state current. Impedance spectrum analyses on the system test rig and a comparison with a short stack experiment have shown that the 300 Hz signal provides plausible results which should contain only a minor deviation from the ideal HFR.

The key variables selected for further analysis are:

1. Stack voltage U_{Stack} and electrical current I;
2. Cathode inlet pressure $p_{ca,in}$ and stoichiometry λ_{ca};
3. Coolant inlet temperature $T_{cool,in}$;
4. High frequency resistance HFR.

In the later sections, these variables will be referred to as Boundary Conditions (BC).

2.2. Test Setup

2.2.1. Fuel Cell Systems

The following analysis is focused on two fuel cell system architectures, System 1 and System 2. Figure 3 describes the subsystems of System 1. Outside the fuel cell system, the power demand was evaluated by the Vehicle Control Unit (VCU). This signal was transferred to the Fuel Cell Control Unit (FCCU), which in turn controls the subsystems to satisfy this demand. Note that due to its almost instantaneous reaction behavior, the Electrical System (ElecS) is not in the scope of this work and was therefore placed outside the system boundary.
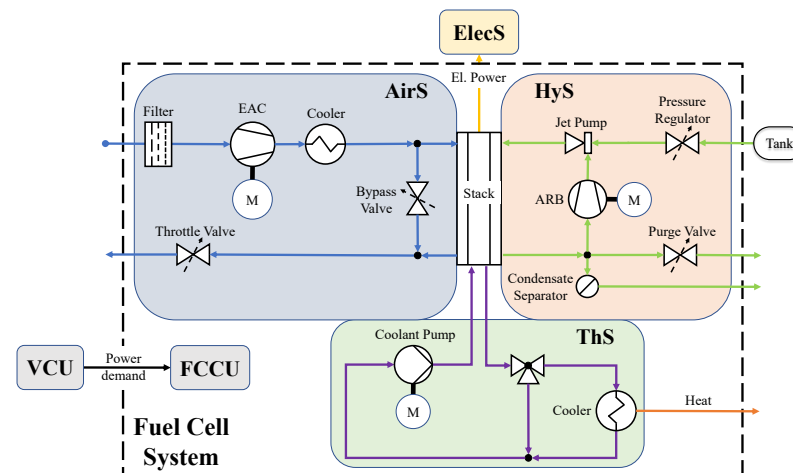

Figure 3. Schematic overview of the main fuel cell system components.

Both fuel cell systems were divided into four subsystems:

*   A 100 kW automotive fuel cell stack, consisting of 370 cells with an active area of approx. 235 cm^2 each. The cells feature an membrane electrode assembly with a 20 µm thick ePTFE-reinforced membrane and gas diffusion layers made of wet-proofed carbon fiber composite paper with a thickness of 200 µm.
*   The AirS, featuring a single stage radial compressor, a cooler and a throttle valve (System 1).
*   The Thermal System (ThS), with its main components coolant pump, cooler with bypass and a 3-way valve.
*   The HyS, with active anode recirculation utilizing a jet pump and an Anode Recirculation Blower (ARB).

While the HyS, ThS and stack were the same in both assemblies, a fundamental change was made within the AirS. A simple AirS was implemented in System 1, where

only an Electric Air Charger (EAC) together with a heat exchanger are utilized. In System 2, the AirS features an additional exhaust turbine and a gas/gas heat exchanger to decrease the electric energy demand for air compression. Note that both systems do not contain a humidifier, resulting in a volume and cost reduction of the systems. Additionally, omitting the humidifier enhances the dynamics of the relative cathode inlet humidity, as the humidifier would add a delay caused by the sorption processes and its additional volume.

2.2.2. Short-Stack Test Rig

Another experiment was carried out on a HORIBA FuelCon Evaluator S5-LT, capable of loads of up to 1000 A, 100 V or 10 kW, with a 15 cell short stack. The cells were the same automotive fuel cells as in the fuel cell systems described beforehand.

2.3. Test Cases

Three test cases were analyzed in detail to show the impact of (1) stack boundary condition adaption, (2) the system architecture and (3) the test rig. The test cases are shown in Table 1 and described in more detail within the following section. Additional boundary conditions for the experiments are given in Appendix A.

Table 1. Overview of test cases.

Case	Description	Load Profile
1a	Adaptive stack boundary conditions	Current steps medium/low load
1b	Fixed stack boundary conditions	Current steps medium/low load
2a	System 1	Synthetic current profile
2b	System 2	Synthetic current profile
3	Short stack	Current increase

3. Results

3.1. Adaptive vs. Fixed Boundary Conditions

The goal of this experiment was to show the impact of the boundary condition adaption on the stack's response. Case 1a is meant to resemble the realistic, vehicle-like operation of the fuel cell stack. Case 1b is a typical experiment found in the literature, where current or voltage variations are performed without an adaption of gas pressure and mass flow [13,16,17].

First, the system was equilibrated at medium load for at least 15 min, until no more changes in the gas and coolant temperatures, mass flows, pressures and relative humidities as well as the stack voltage and HFR were observed. The current was then repeatedly switched between medium and low load. The hold time between the current steps was 5 min. This duration was chosen to observe the targeted dynamic effects on time scales between 0.1 and 100 s while limiting the required test duration. In case 1a, the pressure and stoichiometry of the gas flows were adapted to the current. As the different currents require different optimal pressure and stoichiometry combinations [11], the AirS and the HyS have to be controlled to reach the new set points fast. In case 1b, the mass flow and pressure were kept constant on the set points for the medium load point. The coolant inlet temperature control was set constant to 70 °C in both cases.

Figure 4 shows the resulting boundary conditions and the stacks' response for the cases 1a and 1b. After changes in the current I_{norm}, which was normalized to the rated current of 495 A, minor undershoots and overshoots in the cathode inlet pressure occur in case 1a. In case 1b, the mass flow was kept constant with a high accuracy, leading to a step-like change in cathode stoichiometry. The deviations in the coolant inlet temperature are below 2 K in both cases.
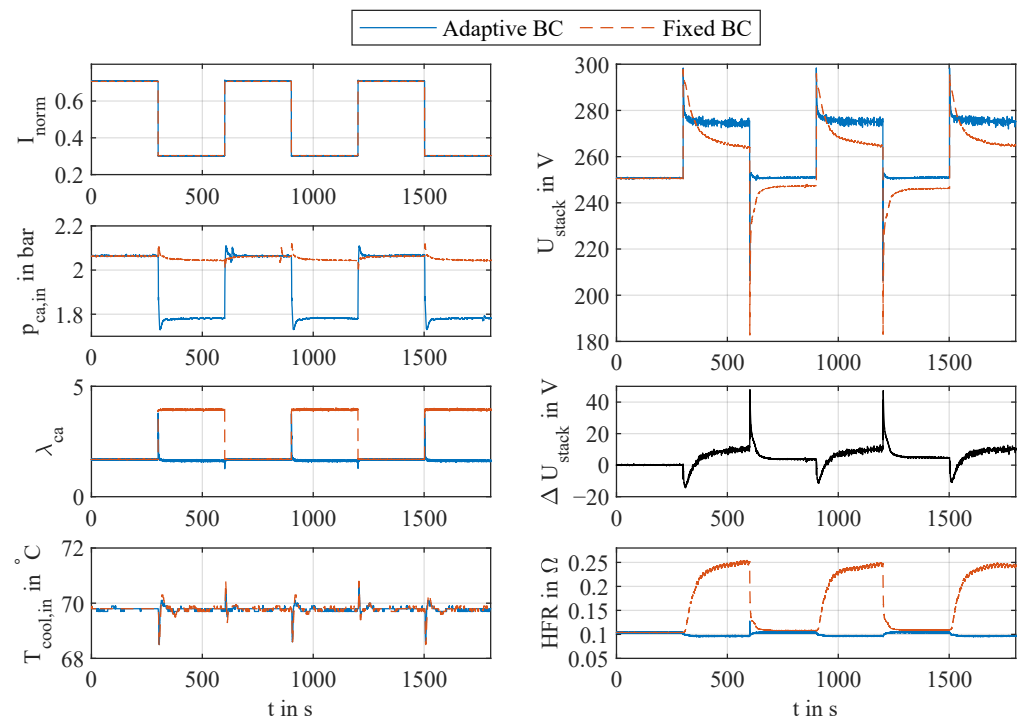
Figure 4. Stack boundary conditions and response in case 1a (adaptive boundary conditions) and 1b (fixed boundary conditions).

The stack voltage response, HFR and the difference between the stack voltages ΔU_{stack} in cases 1a and 1b are also depicted. Significant stack voltage overshoots of $\approx$25 V and undershoots of up to 60 V in case 1b are visible. Furthermore, a significantly slower adaption to the new stationary voltage occurs in case 1b compared to case 1a. In case 1b, the stack voltage approaches lower stationary values due to increased ohmic losses, as the HFR more than doubles.

3.2. System Architecture Comparison

A synthetic current profile was selected to evaluate the differences between the two systems described in Section 2.2.1. The load profile features upward and downward current steps of varying amplitude, with constant current phases in between. The ThS control was set to a constant coolant inlet temperature of 60 °C. The gas mass flow and pressure set points were current dependent. The operating strategy differs between the systems, as component limitations restrict the achievable mass flow and pressure set points differently.

Figure 5 shows the boundary conditions and resulting stack response for cases 2a and 2b. Note that the pressure and stoichiometry set points were adapted to the system's capabilities and the surge limit of the EAC. This adaption leads to a higher operating pressure and a lower stoichiometry in System 1 most of the time. Additionally, the current profile was slightly changed in magnitude to produce almost the same stack voltage, but the impact on the targeted dynamics should be negligible. In case 2b (System 2), large spikes in the cathode stoichiometry after downward current steps were measured. The coolant inlet temperature was the same for both measurements.
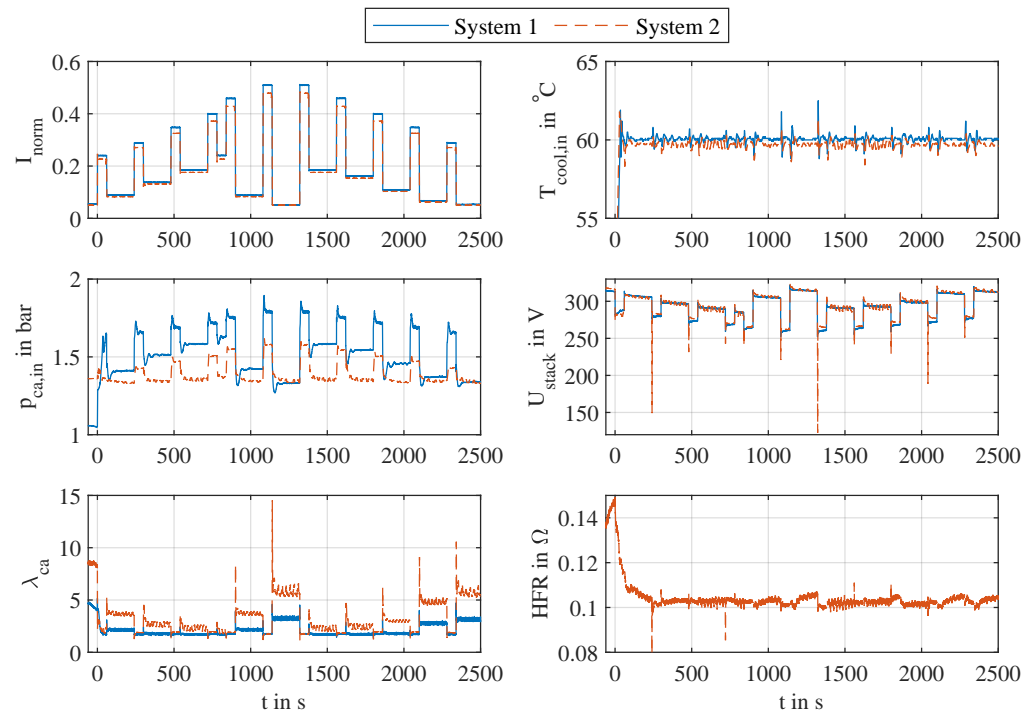
Figure 5. Stack boundary conditions and response during load profile in case 2a (System 1) and 2b (System 2).

As intended, the stack voltage is almost the same during the stationary current phases. However, large deviations occur in the dynamic response, with deep undershoots of up to ≈140 V in case 2b. The zoom-in in Figure 6 focuses on this prominent behavior. The HFR is only measured for System 2 and shows almost constant values, suggesting a good hydration, except for the initial low load phase. Note that the spikes in the HFR signal during current steps are artifacts of the data collection process.
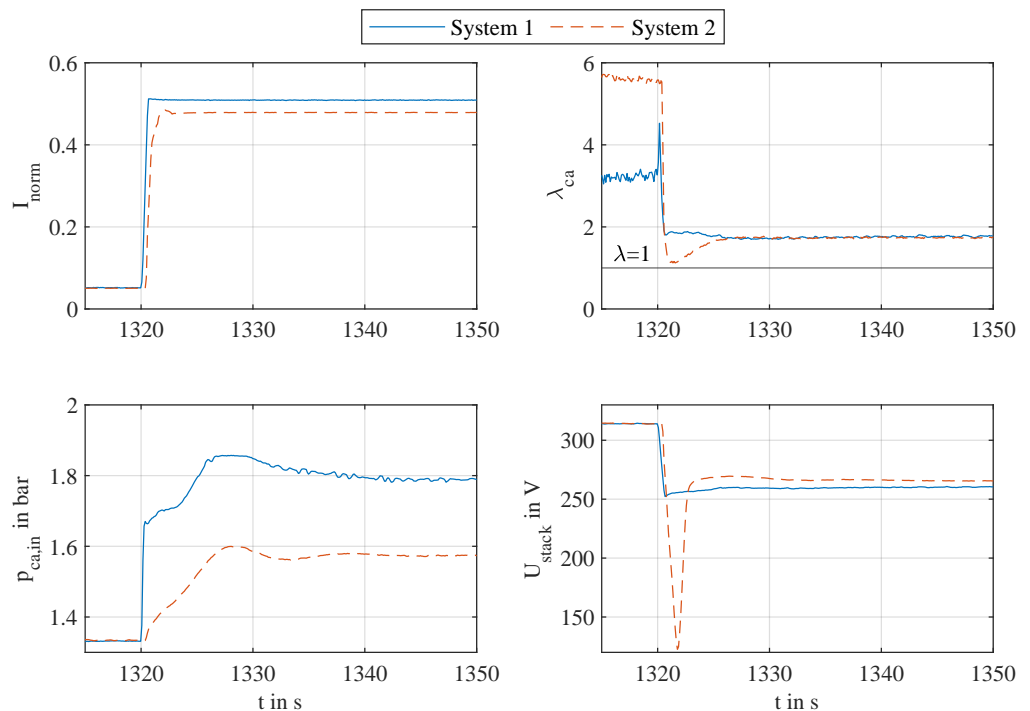

Figure 6. Zoom-in of boundary condition adaption and stack response during current increase in case 2a (System 1) and 2b (System 2), showing partial oxygen starvation.

In Figure 6, the slower mass flow dynamics of System 2 are visible. The undershoot in stoichiometry down to almost 1, as marked by the horizontal black line, suggests a period of partial oxygen starvation due to limited diffusion as a cause for the deep voltage undershoot. An impact of the gas flow on the water transport is unlikely to be the main factor for the voltage undershoot, as liquid water accumulation usually requires more time and the voltage undershoot ends right as the stoichiometry is no longer critically low. The quick reaction time of System 1's AirS results in an almost step-like initial increase of the pressure and no critical undershoot in stoichiometry.

3.3. Short Stack Experiment

Multiple stationary operating points with a hold time of 15 min each were set. The current was ramped down linearly to 0 A within 100 s after each stationary operating point and the gas inlet conditions were adapted to the next operating point. After a no-current phase of 100 s, the current was ramped up again. This procedure was originally developed to conduct stationary tests while respecting the limited dynamic capabilities of the test rig between two operating points. The analysis in Section 3.3 is focused on one current ramp-up and the following equilibration phase from the test run.

Figure 7 shows the short stacks' voltage response to an increase in normalized current I_{norm}. Note that the equivalent voltage $U_{stack,eq}$ is based on a scale-up to the number of cells in the full stack used in the other experiments. Compared to the cases described beforehand, the increase of current is rather slow. The voltage undershoot shows a very long relaxation time, while a constant air mass flow $\dot{m}_{air}$ and cathode inlet pressure are achieved. The coolant inlet temperature approaches the stationary value significantly slower than in the system test rig experiments.

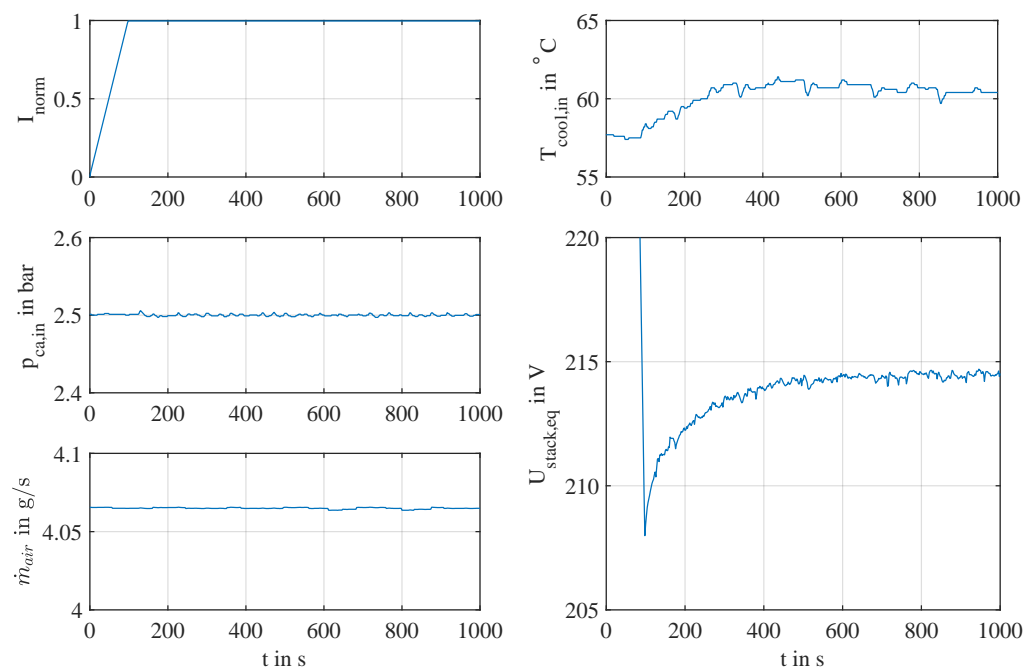**Figure 7.** Stack boundary conditions and response during load profile in case 3 (short stack).

3.4. Comparison

A comparison of the time constants τ of the boundary conditions and the voltage response allows us to analyze the dominating process path (see Figure 2) for the voltage under- and overshoot behavior. The time constant is evaluated by fitting the function

$$f_1(t) = C_1 exp(-t/\tau) + C_2 \tag{1}$$

to each time-dependent signal $y(t)$ between the current changes, using a weighted least squares method. The weights w_i are varied linearly between 1 and 0, emphasizing the initial response behavior. The objective is to minimize $g(C_1, \tau, C_2)$ by varying the parameters C_1, τ, C_2 with

$$g(C_1, \tau, C_2) = \sum_{i=1}^{N_{sample}} w_i(y(t_i) - f(t_i))^2. \tag{2}$$

As the signals' shapes differ from each other, it is challenging to find a common definition for the time constant calculation. The voltage, HFR and stoichiometry show good agreement with the selected fitting function. The inlet pressure can also be fitted, but minor over- and undershoots of 2–3% with a peak time of 8–11 s occur, e.g., in case 1a. This yields a small error when evaluating the fitting function.

In cases 1 and 2, the coolant temperature behaves differently and cannot be approximated with the fitting function from Equation (1). Therefore, a settling time with an error band of 0.5 K is calculated for comparison.

The time constants evaluated from cases 1–3 are differentiated between upward and downward current steps and are shown in Tables 2 and 3. In case 1b, the mass flow was kept constant with a very low error below 1.5%. Therefore, no useful time constant can be derived and the entry is marked as constant. This is also true for the pressure and mass flow behavior in case 3. In cases 2a and 3, no HFR measurement was taken. The entry is marked as not available (n.a.). A few outliers with a large deviation, especially in case 2, were neglected for further analysis. In case 2b, no sound fitting was achieved for the HFR signal and the according entry is therefore marked with -.

Table 2. Fitted time constants after current increases in seconds. (*) Settling time instead of time constant is displayed.

Case	τ_U	τ_{HFR}	τ_p	τ_λ	τ_T
1a	0.2	10.9–11.0	0.9	1.9	5.6–6.4 *
1b	11.1–11.7	10.0–11.0	6.6–6.7	const.	6.7 *
2a	1.8–6.3	n.a.	0.9–2.7	0.1–2.6	7.5–18.3 *
2b	0.3–1.1	-	2.1–4.2	1.3–3.5	6.6–17.0 *
3	115	n.a.	const.	const.	103

Table 3. Fitted time constants after current decreases in seconds. (*) Settling time instead of time constant is displayed.

Case	τ_U	τ_{HFR}	τ_p	τ_λ	τ_T
1a	3.9–4.2	19.1–19.5	1.5	1.5	7.5–7.7 *
1b	40.9–46.0	41.7–48.8	12.5–13.2	const.	9.5–10.0 *
2a	1.9–5.0	n.a.	0.8–3.9	0.2–0.6	7.5–19.3 *
2b	12.7–30.1	-	7.0–23.8	0.9–8.5	6.7–15.0 *

Cases 1a and 1b show high reproducibility, as the range of the calculated time constants is low. After current increase, the voltage response time τ_U is around 60 times lower if the boundary conditions are adapted in case 1a with respect to the fixed BC case 1b. After a current decrease, τ_U is around ten times smaller in case 1a compared to case 1b. It has to be highlighted that the voltage response in case 1b matches the HFR dynamics very well. In case 1a, the voltage dynamics are in the order of magnitude of the gas supply response times, but no clear correlation can be identified. Note that in case 1a, neither the temperature nor the HFR dynamics match with the voltage response times.

The system comparison shows that System 1 adapts faster to new pressure and stoichiometry set points than System 2 with its slower, more complex air system. This is mainly caused by the addition of the turbine in the air system, which has a significant inertia and therefore takes time to be sped up by the gas flow. As a result, the mass flow

and pressure build-up are delayed. Generally, the range of calculated response times grows as the operating range and current step size are increased in the load profile compared to case 1. While τ_U is comparable between current increase and decrease in System 1, an asymmetry between both steps is visible in System 2. The significantly slower response time τ_U of System 2 after a current decrease is linked to the slower pressure dynamics.

The short stack experiment in case 3 shows, by far, the slowest response times τ_U. A similarly slow temperature adaption is visible. The cathode pressure and mass flow are constant.

4. Discussion

The process chain from Figure 2 is broken down to the dominating effects for three selected cases according to the results presented in this paper, see Figure 8. Test case 1 shows two different voltage relaxation modes, which can be distinguished by their dominating effect: With adaptive boundary conditions, the stack voltage reacts with a time constant similar to the ones of the air supply. The ohmic resistance is almost constant, thereby suggesting only a small change in membrane humidity. The change in voltage is therefore linked to the local partial pressure dynamics of the reactants.
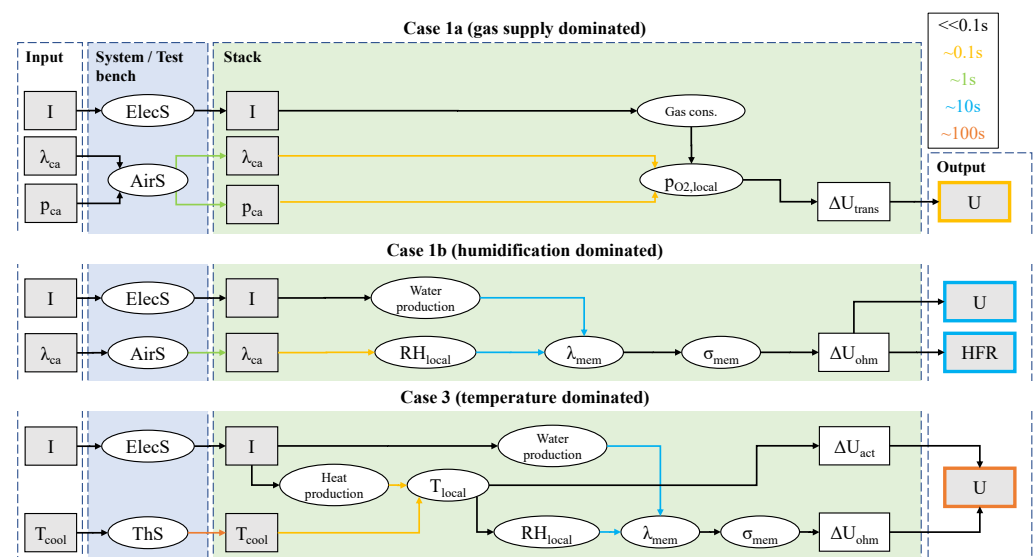

Figure 8. Process chain showing dominating effects, their interaction and typical time-scales in selected experimental cases.

If the gas supply is kept constant, the voltage response is dominated by the membrane humidification and dry-out, resulting in varying ohmic resistance. The time constants of the HFR signal and the stack voltage match well. The loss in membrane conductivity is linked to dry-out: while the air mass flow remains high, the current and the resulting water production are reduced by ≈60%. Additionally, the HFR does not return completely to the stationary value from case 1a within 5 min. A slow component of the rehydration process with a time constant above 5 min prevents the voltage from reaching the initial steady-state again. The initially higher voltage after a current decrease is caused by the higher reactant partial pressure, but is then overcompensated by the increase in ohmic resistance. After the dry phase, the undershoot increases in depth as expected. This can be prevented with an adapted operating strategy that ensures minimal variation in membrane water content.

Analyzing the HFR time constants, the rehydration process is approximately four times faster than the dehydration process. This is not in line with results from Didierjean et al. [26], which calculated water desorption kinetics to be five times faster than the adsorption kinetics from the gas phase for Nafion 117. Furthermore, they modeled and measured significantly lower time constants well above 100 s. It is likely that the different experimental setup caused this discrepancy. Didierjean et al. [26] used a membrane in a

controlled environment, without an active fuel cell reaction, to measure the sorption kinetics. In the experiments described in this work, the fuel cell reaction is ongoing. Another possible explanation might be that the adsorption process is dominated by liquid water uptake. Zawodzinski et al. [5] measured lower time constants when immersing a Nafion 117 membrane in liquid water compared to water uptake from the gas phase [26].

Different system architectures and components limit the achievable set points and dynamics for pressure and stoichiometry. The operating strategy may need adaption to the actual system and vice versa. The mass flow dynamics is especially one key limitation to the achievable current dynamics. Deeper undershoots occur in System 2, caused by its lower mass flow dynamics. In the case of a reactant starvation, a significant voltage reduction is observed. This state has to be avoided to satisfy the power demand and reduce aging [12].

Typical short stack test rigs are limited in the achievable gas supply dynamics and the thermal control response time. A significantly slower voltage response time of ≈100 s was measured. The time constant analysis suggests that this response is dominated by the slow thermal control, possibly in combination with a membrane humidification process. The latter can only be presumed based on the other experiments, as no HFR measurement is available from this specific test.

The transient voltage response of the stack can be influenced via the operating strategy, system architecture and/or the test rig. Three dominating effects are identified from the experiments:

1. Air supply (pressure and stoichiometry) with typical time constants between 0.9 s and 1.9 s;
2. Membrane hydration and dehydration with typical time constants of ≈10 s and ≈45 s, respectively;
3. The coolant inlet temperature dynamics, which have typical settling times of ≈7–15 s in realistic automotive systems, but time constants around ≈100 s on a common short stack test rig.

The impact of the anode loop on the observed dynamic response characteristics is assumed to be negligible, as the HyS reacts fast to changes in the set points. In addition, the anode mass flows and their resulting impact on membrane humidification are small compared to the cathode side. During the case 1b experiment, the cathode dry-out caused a decreasing relative humidity within the anode loop, which did not occur in case 1a. A possible impact of changing gas composition within the anode loop on the voltage response could not be observed.

5. Conclusions

Matching the system and/or test rig dynamic capabilities with the application is important to ensure realistic and transferable testing. Typical short stack test rigs are not suited for the development and verification of dynamic operating strategies. The results highlight the gap between steady-state or low-dynamic component testing and the automotive application of a fuel cell dominant vehicle. This gap needs to be bridged by targeted research and appropriate systems engineering to successfully implement fuel cell systems in future vehicles.

From a scientific point of view, it is of the utmost importance to evaluate the test setup and its influence carefully when conducting dynamic experiments to avoid the misinterpretation of results, as the dominating effects are heavily test case dependent. For practical applications, test rigs or test systems with application-like dynamic characteristics are the key to improving the system's control strategy for automotive application. Complete stand-alone systems would offer smaller packaging volume and therefore more realistic pipe lengths and lower heat losses resulting in increased dynamics and better enthalpy recuperation of the turbine, but they offer less space for sensor installation and swapping components becomes more challenging.

The experimental data will be useful for validating stack models and for parametrizing power split optimization models with realistic component reaction times. While this work focused on unhumidified systems, it is expected that humidified systems react slower to load changes due to the humidifier dynamics. Developing a suited strategy for the highly dynamic operation of a humidified system will therefore be more complex.

Additional research should be focused on broadening the experimental data basis available from application-like systems and the cross-checking of dynamic simulation models, which might not have been validated by sufficiently dynamic experiments.

Author Contributions: Conceptualization, J.B. and M.H.; methodology, J.B. and M.H.; software, J.B.; validation, J.B.; formal analysis, J.B.; investigation, J.B.; resources, H.K.; writing—original draft preparation, J.B.; writing—review and editing, J.B., M.H., H.K. and S.K.; visualization, J.B.; supervision, H.K. and S.K.; project administration, H.K.; funding acquisition, H.K. All authors have read and agreed to the published version of the manuscript.

Abbreviations

The following abbreviations are used in this manuscript:

AirS	Air System
ARB	Anode Recirculation Blower
BC	Boundary Conditions
DoE	Department of Energy
EAC	Electric Air Charger
ElecS	Electrical System
EUCAR	European Council for Automotive R&D
FCS	Fuel Cell System
FCCU	Fuel Cell Control Unit
HFR	High Frequency Resistance
HyS	Hydrogen System
PEM	Polymer Electrolyte Membrane
PEMFC	Polymer Electrolyte Membrane Fuel Cell
PHEV	Plug-in Hybrid Electric Vehicle
ThS	Thermal System
VCU	Vehicle Control Unit
WLTC	Worldwide harmonized Light vehicles Test Cycle

Appendix A

The additional boundary conditions selected for the test cases are typical for automotive operation and are shown in Tables A1–A3. For each parameter, the measured mean value and standard deviation is displayed. Note that in the cases 1 and 2, where a fuel cell system is used, not all stack inlet conditions are controlled directly and may change significantly over time during dynamic operation.

Table A1. Boundary conditions for test case 1.

Parameter	Value		Unit
	Case 1a	Case 1b	
I_{norm}	See Figure 4		-
p_{amb}	0.9800 ± 0.0001	0.9800 ± 0.0001	bar
T_{amb}	20.83 ± 1.57	20.99 ± 0.28	°C
RH_{amb}	40.74 ± 3.96	40.06 ± 1.43	%
$p_{ca,in}$	See Figure 4		bar
λ_{ca}	See Figure 4		$\mathrm{g\,s^{-1}}$
$p_{an,in} - p_{ca,in}$	0.247 ± 0.029	0.252 ± 0.029	bar
$T_{cool,in}$	See Figure 4		°C
ΔT_{cool}	5.30 ± 0.48	5.26 ± 0.71	K

Table A2. Boundary conditions for test case 2.

Parameter	Value		Unit
	Case 2a	Case 2b	
I_{norm}	See Figure 5		-
p_{amb}	0.9800 ± 0.0002	0.9800 ± 0.0001	bar
T_{amb}	20.96 ± 0.77	20.99 ± 0.59	°C
RH_{amb}	42.21 ± 6.16	40.65 ± 2.67	%
$p_{ca,in}$	See Figure 5		bar
λ_{ca}	See Figure 5		$\mathrm{g\,s^{-1}}$
$p_{an,in} - p_{ca,in}$	0.141 ± 0.035	0.175 ± 0.048	bar
$T_{cool,in}$	See Figure 5		°C
ΔT_{cool}	3.89 ± 2.21	3.65 ± 1.65	K

Table A3. Boundary conditions for test case 3.

Parameter	Value	Unit
I_{norm}	See Figure 7	-
$p_{ca,in}$	See Figure 7	bar
$T_{ca,in}$	59.99 ± 0.05	°C
$RH_{ca,in}$	16.15 ± 0.07	%
$\dot{m}_{air}$	See Figure 7	$\mathrm{g\,s^{-1}}$
$p_{an,in}$	2.500 ± 0.004	bar
$T_{an,in}$	59.94 ± 0.05	°C
$RH_{an,in}$	87.57 ± 0.20	%
$\dot{m}_{H_2}$	0.122 ± 0.000	$\mathrm{g\,s^{-1}}$
$T_{cool,in}$	See Figure 7	°C
ΔT_{cool}	11.80 ± 2.73	K

The cathode inlet temperature is a result of the cooler temperature and the cathode inlet pressure. The cathode inlet humidity depends on the ambient humidity, the cathode inlet pressure and the cathode inlet temperature, as no humidifier is implemented. The anode inlet temperature is influenced by the mixture ratio between recirculated gas and fresh hydrogen and the temperatures of each gas flow. The anode inlet humidity is a result of the recirculation mass flow, the fresh hydrogen mass flow, the anode outlet humidity and the purge strategy. The anode stoichiometry depends on the fresh hydrogen mass flow, the recirculation mass flow and the purge strategy.

References

1. Release Hyundai ix35 Fuel Cell. Available online: https://www.hyundai.com/worldwide/en/company/newsroom/hyundai-ix35-fuel-cell-0000001596 (accessed on 2 August 2022).
2. Toyota Ushers in the Future with Launch of 'Mirai' Fuel Cell Sedan. Available online: https://global.toyota/en/detail/4198334 (accessed on 30 June 2022).

3. DOE Technical Targets for Fuel Cell Systems and Stacks for Transportation Applications. Available online: https://www.energy.gov/eere/fuelcells/doe-technical-targets-fuel-cell-systems-and-stacks-transportation-applications (accessed on 30 June 2022).
4. Ye, X.; Wang, C.Y.; Ye, X.; Wang, C.-Y. Measurement of Water Transport Properties Through Membrane-Electrode Assemblies. *J. Electrochem. Soc.* **2007**, *154*, B676. [CrossRef]
5. Zawodzinski, T.A.; Derouin, C.; Radzinski, S.; Sherman, R.J.; Smith, V.T.; Springer, T.E.; Gottesfeld, S. Water Uptake by and Transport Through Nafion® 117 Membranes. *J. Electrochem. Soc.* **1993**, *140*, 1041–1047. [CrossRef]
6. Springer, T.E.; Zawodzinski, T.A.; Gottesfeld, S. Polymer electrolyte fuel cell model. *J. Electrochem. Soc.* **1991**, *138*, 2334. [CrossRef]
7. Weber, A.Z.; Newman, J. Transport in Polymer-Electrolyte Membranes. *J. Electrochem. Soc.* **2004**, *151*, A311. [CrossRef]
8. Knights, S.D.; Colbow, K.M.; St-Pierre, J.; Wilkinson, D.P. Aging mechanisms and lifetime of PEFC and DMFC. *J. Power Sources* **2004**, *127*, 127–134. [CrossRef]
9. Battery Requirements for Future Automotive Applications. Available online: https://www.eucar.be/battery-requirements-for-future-automotive-applications/ (accessed on 1 October 2022).
10. Lohse-Busch, H.; Duoba, M.; Stutenberg, K.; Iliev, S.; Kern, M.; Richards, B.; Christenson, M.; Loiselle-Lapointe, A. *Technology Assessment of a Fuel Cell Vehicle: 2017 Toyota Mirai*; Argonne National Lab.: Argonne, IL, USA, 2018.
11. Hellmann, M. *Robuste Auslegung von Mobilen Brennstoffzellensystemen*; TEWISS-Techn. und Wissen GmbH: Garbsen, Germany, 2014.
12. Ren, P.; Pei, P.; Li, Y.; Wu, Z.; Chen, D.; Huang, S. Degradation mechanisms of proton exchange membrane fuel cell under typical automotive operating conditions. *Prog. Energy Combust. Sci.* **2020**, *80*, 100859. [CrossRef]
13. Cho, J.; Kim, H.S.; Min, K. Transient response of a unit proton-exchange membrane fuel cell under various operating conditions. *J. Power Sources* **2008**, *185*, 118–128. [CrossRef]
14. Loo, K.; Wong, K.; Tan, S.; Lai, Y.; Tse, C.K. Characterization of the dynamic response of proton exchange membrane fuel cells—A numerical study. *Int. J. Hydrogen Energy* **2010**, *35*, 11861–11877. [CrossRef]
15. Wang, Y.; Wang, C.Y. Transient analysis of polymer electrolyte fuel cells. *Electrochim. Acta* **2005**, *50*, 1307–1315. [CrossRef]
16. Peña Arias, I.K.; Trinke, P.; Hanke-Rauschenbach, R.; Sundmacher, K. Understanding PEM fuel cell dynamics: The reversal curve. *Int. J. Hydrogen Energy* **2017**, *42*, 15818–15827. [CrossRef]
17. Weydahl, H.; Møller-Holst, S.; Børresen, B. Effect of gas composition and gas utilisation on the dynamic response of a proton exchange membrane fuel cell. *J. Power Sources* **2008**, *180*, 808–813. [CrossRef]
18. Tang, Y.; Yuan, W.; Pan, M.; Li, Z.; Chen, G.; Li, Y. Experimental investigation of dynamic performance and transient responses of a kW-class PEM fuel cell stack under various load changes. *Appl. Energy* **2010**, *87*, 1410–1417. [CrossRef]
19. Loskutov, A.; Kurkin, A.; Shalukho, A.; Lipuzhin, I.; Bedretdinov, R. Investigation of PEM Fuel Cell Characteristics in Steady and Dynamic Operation Modes. *Energies* **2022**, *15*, 6863. [CrossRef]
20. San Martín, I.; Ursúa, A.; Sanchis, P. Modelling of PEM Fuel Cell Performance: Steady-State and Dynamic Experimental Validation. *Energies* **2014**, *7*, 670–700. [CrossRef]
21. Edwards, R.L.; Demuren, A. Regression analysis of PEM fuel cell transient response. *Int. J. Energy Environ. Eng.* **2016**, *7*, 329–341. [CrossRef]
22. Li, X.; Han, K.; Song, Y. Dynamic behaviors of PEM fuel cells under load changes. *Int. J. Hydrogen Energy* **2020**, *45*, 20312–20320. [CrossRef]
23. Kim, S.; Shimpalee, S.; Van Zee, J. The effect of stoichiometry on dynamic behavior of a proton exchange membrane fuel cell (PEMFC) during load change. *J. Power Sources* **2004**, *135*, 110–121. [CrossRef]
24. Tang, W.; Lin, R.; Weng, Y.; Zhang, J.; Ma, J. The effects of operating temperature on current density distribution and impedance spectroscopy by segmented fuel cell. *Int. J. Hydrogen Energy* **2013**, *38*, 10985–10991. [CrossRef]
25. Dicks, A.; Rand, D.A.J. *Fuel Cell Systems Explained*, 3rd ed.; Topics in Applied Physics; Wiley: Hoboken, NJ, USA, 2018; Volume 113.
26. Didierjean, S.; Perrin, J.; Xu, F.; Maranzana, G.; Klein, M.; Mainka, J.; Lottin, O. Theoretical evidence of the difference in kinetics of water sorption and desorption in Nafion® membrane and experimental validation. *J. Power Sources* **2015**, *300*, 50–56. [CrossRef]